System Identification for eVTOL Aircraft Using Simulated Flight Data

Benjamin M. Simmons*
NASA Langley Research Center, Hampton, Virginia 23681

This paper describes a system identification method for electric vertical takeoff and landing (eVTOL) aircraft. The approach merges fixed-wing and rotary-wing modeling techniques with new strategies to develop a modeling method for eVTOL vehicles using flight test data. The eVTOL aircraft system identification approach is demonstrated through application to the NASA LA-8 tandem tilt-wing, distributed electric propulsion aircraft using a high-fidelity flight dynamics simulation. Orthogonal phase-optimized multisine inputs are applied to each control surface and propulsor at numerous flight conditions throughout the flight envelope to collect informative flight data. An aero-propulsive model is identified at each flight condition using the equation-error method in the frequency domain. The local model parameters are then blended to create a global model across the nominal flight envelope. Parameter estimation results are shown to provide a good fit to modeling data and have good prediction capability. The methodology is developed with a discussion of unique eVTOL vehicle aerodynamic characteristics and practical strategies intended to inform future flight-based system identification efforts for eVTOL aircraft.

Nomenclature

a_x, a_y, a_z = body-axis translational acceleration, ft/s^2
g = gravitational acceleration, ft/s^2
h_x, h_y, h_z = net body-axis propulsion system angular momentum, slug-ft^2/s
I_x, I_y, I_z, I_{xz} = moments of inertia, slug-ft^2
L, M, N = body-axis aero-propulsive moments, ft-lbf
m = aircraft mass, slug
n_1, n_2,..., n_8 = LA-8 propulsor rotational speeds, revolutions/s
p, q, r = body-axis angular velocity components, rad/s or deg/s
u, v, w = body-axis translational velocity components, ft/s
V = true airspeed, ft/s
X, Y, Z = body-axis aero-propulsive forces, lbf
α = angle of attack, rad or deg
β = angle of sideslip, rad or deg
δ_{e_1}, δ_{e_2}, δ_{e_3}, δ_{e_4} = LA-8 elevon deflections, rad or deg
δ_{f_1}, δ_{f_2}, δ_{f_3}, δ_{f_4} = LA-8 flap deflections, rad or deg
δ_{r_1}, δ_{r_2} = LA-8 ruddervator deflections, rad or deg
δ_{w_1}, δ_{w_2} = LA-8 front and rear wing angles, rad or deg
ϕ, θ, ψ = Euler roll, pitch, and yaw angles, rad or deg
ρ = air density, slug/ft^3

Superscripts
^{T} = transpose
$^{-1}$ = matrix inverse
$\hat{}$ = estimate
$\dot{}$ = time derivative
$\tilde{}$ = Fourier transform
† = complex conjugate transpose

---

*Research Engineer, Flight Dynamics Branch, MS 308, Member AIAA.

I. Introduction

Enabling technologies for the introduction of Urban Air Mobility (UAM) as a future transportation method are a research focus across the aerospace industry. Many electric vertical takeoff and landing (eVTOL) aircraft configurations are being developed* as transitioning vehicles able to precisely execute low-speed maneuvers in a congested urban air traffic system while also leveraging an efficient, high-speed cruise flight mode. The broadened aeronautical vehicle design space, uniquely utilizing distributed propulsion technology, has resulted in a diverse set of eVTOL configurations including tilt-wings, tilt-rotors, and lift+cruise (dual propulsion system) concepts [1–6]. These novel designs have formed a new category of aircraft that are a hybrid between fixed-wing and rotary-wing aircraft, but also exhibit unique configuration-specific phenomena.

Many eVTOL aircraft research areas require further study prior to introduction of operational vehicles in a UAM air traffic system. These areas include flight controls strategies, airworthiness certification, handling qualities, contingency management, vehicle autonomy, and air traffic management. Accurate vehicle aerodynamic models are essential for eVTOL aircraft flight dynamics simulations enabling flight control system development and certification activities. Since propulsion aerodynamics, airframe aerodynamics, and propulsion-airframe interactional aerodynamics are generally highly coupled for eVTOL aircraft, their aerodynamic models represent a combination of propulsion and airframe aerodynamics characteristics that must be modeled together. For this reason, eVTOL aircraft aerodynamic models can also be referred to as aero-propulsive models.

Previous research has investigated methods for efficient eVTOL aircraft aero-propulsive modeling across their wide flight envelopes using computational fluid dynamics (CFD) simulations [7, 8] and wind tunnel testing [9–13]. References [8, 11] justified the use of tilt-wing and lift+cruise eVTOL aircraft-specific modeling procedures. CFD aerodynamic characterization studies are advantageous because they allow analysis in early design stages, where the aircraft configuration is not yet finalized and vehicle hardware has not yet been developed. Wind tunnel studies require a test asset, but allow efficient, high-fidelity vehicle characterization in a low-risk test environment. The disadvantages of CFD include necessary simplifying assumptions to make calculations computationally tenable and flowfield models which may not adequately reflect real flight vehicle aerodynamics, particularly for modeling complex flowfields of eVTOL aircraft. One disadvantage of wind tunnel testing is the presence of sting and wall effects. Also, the general requirement of using subscale models for wind tunnel testing requires using similitude relationships to scale the results, which are challenging for rotorcraft and typically limit vehicle wind tunnel testing [14, 15].

A goal of an aircraft aerodynamic model is to accurately describe the aerodynamics in flight, which drive aircraft flight dynamic behavior. Thus, aerodynamic characterization using flight data offers the closest prediction to operational reality. This work builds on previous CFD and wind tunnel eVTOL aircraft modeling studies [8, 11] to propose a method for flight-based aero-propulsive model development. The process of developing mathematical models describing aircraft motion from measured input and output data is referred to as aircraft system identification [16–18]. The aircraft system identification process generally involves identifying a mathematical representation of the applied forces and moments as a function of state and control variables, based on experimental data. Fixed-wing aircraft and rotorcraft generally follow different modeling conventions, but their system identification techniques are well-developed for standard problems and have been applied successfully to numerous aircraft configurations [16–22].

Although eVTOL aircraft share aerodynamic characteristics overlapping with both fixed-wing and rotary-wing aircraft, system identification approaches used for either type of vehicle do not directly translate to modeling eVTOL vehicles. eVTOL aircraft aerodynamic modeling is also challenging due to the presence of many control surfaces and propulsors, propulsion-airframe interactions, high incidence angle propulsor aerodynamics, vehicle instability, rapidly changing aerodynamics through transition, and large flight envelopes that need to be characterized by a global aero-propulsive model. This work proposes an aircraft system identification process tailored to eVTOL aircraft based on their unique aerodynamic characteristics and extends global modeling techniques used in previous fixed-wing aircraft research [23]. System identification maneuvers are executed sequentially starting from trimmed flight conditions throughout transition and modeling is performed using the equation-error method in the frequency domain at each reference condition in post-flight analysis. The approach is formulated using simulated flight data, but can be applied to future flight test aircraft system identification efforts. The input design, signal processing, and parameter estimation methods used for this work were from the System IDentification Programs for AirCraft (SIDPAC) software toolbox.†

The paper is organized as follows: Section II provides an overview of the eVTOL aircraft flight dynamics simulation used to perform simulated flight testing. Section III describes the proposed eVTOL aircraft aero-propulsive modeling framework, followed by a description of the flight test experimental design techniques needed to collect data for model

---

*Information available online at https://evtol.news/aircraft [retrieved 8 October 2021]

†Information available online at https://software.nasa.gov/software/LAR-16100-1 [retrieved 8 October 2021].

identification in Sec. IV. Section V gives an overview of the employed parameter estimation methods. Section VI provides sample local and global modeling results. Overall conclusions are summarized in Sec. VII.

II. eVTOL Aircraft Simulation

The system identification approach proposed in this paper is exercised for a tandem tilt-wing eVTOL vehicle in a MATLAB®/Simulink® generalized UAM-class vehicle simulation developed at NASA Langley Research Center [24]. The high-fidelity simulation environment contains both common, aircraft-agnostic simulation components and aircraft-specific model components, which provides a flexible framework for algorithm development for multiple eVTOL vehicle configurations. The vehicle equations of motion, numerical integrators, and the atmospheric model are common to all vehicles. Each vehicle model, which includes the aero-propulsive model, actuator models, inertial properties, and control laws, is implemented in a modular framework to enable simultaneous assessment of multiple vehicles.

A. Flight Dynamics Simulation Framework

Nonlinear vehicle simulations are performed using the kinematic and dynamic aircraft equations of motion developed under a standard set of assumptions [16, 25, 26]. The aircraft is modeled as a six degree-of-freedom rigid body, treating the gyroscopic effects from the rotating portions of the propulsion system as applied external moments. Applied forces (X, Y, Z) and moments (L, M, N) are computed using the vehicle aero-propulsive model, which includes the collective contributions of propulsion and airframe effects as well as their interactions. The translational dynamics equations are:

$$\dot{u} = rv - qw - g\sin\theta + X/m \tag{1}$$

$$\dot{v} = pw - ru + g\cos\theta\sin\phi + Y/m \tag{2}$$

$$\dot{w} = qu - pv + g\cos\theta\cos\phi + Z/m \tag{3}$$

The rotational dynamics equations augmented to include propulsor gyroscopic effects are:

$$I_x\dot{p} - I_{xz}\dot{r} = L + (I_y - I_z)qr + I_{xz}pq - (\dot{h}_x + qh_z - rh_y) \tag{4}$$

$$I_y\dot{q} = M + (I_z - I_x)pr + I_{xz}(r^2 - p^2) - (\dot{h}_y + rh_x - ph_z) \tag{5}$$

$$I_z\dot{r} - I_{xz}\dot{p} = N + (I_x - I_y)pq - I_{xz}qr - (\dot{h}_z + ph_y - qh_x) \tag{6}$$

The angular momentum of a single propulsor about its axis of rotation is $h_p = I_p\Omega_p$, where I_p is the moment of inertia of the rotating portion of the propulsor and $\Omega_p = 2\pi n$ is the rotation rate in radians per second, with clockwise rotation when viewed from behind the rotating propulsor being positive. For use in the above equations, the angular momentum for each propulsor is rotated into the aircraft body axes and then summed to compute the net angular momentum for all propulsors $(h_x,\ h_y,\ h_z)$ [27]. Computing the net rate of change of angular momentum $(\dot{h}_x,\ \dot{h}_y,\ \dot{h}_z)$ follows the same process. If the propulsors are operated symmetrically, their angular momentum components cancel; however, asymmetric propulsor operation necessary for system identification causes the propulsion gyroscopic effects to become significant.

The aircraft equations of motion are also augmented with additional states to represent the dynamics associated with control surface actuation and propulsor speed changes. Lag associated with the propulsors are particularly important to consider for controller design because propulsion dynamics can be significantly slower than control surface dynamics, particularly for eVTOL vehicles with fixed-pitch propellers. For this work, propulsor and control surface dynamics were modeled using first-order and second-order dynamics, respectively, representing the lag between a commanded value and actual value. Expressed as a differential equation, these respectively take the form,

$$\tau\dot{\delta} + \delta = \delta_{\text{cmd}} \tag{7}$$

$$\ddot{\delta} + 2\zeta\omega_n\dot{\delta} + \omega_n^2\delta = \omega_n^2\delta_{\text{cmd}} \tag{8}$$

where δ is the actual value of a propulsor or control surface variable, δ_{cmd} is the corresponding commanded value, τ is the first-order time constant, ω_n is the natural frequency, and ζ is the damping ratio.

eVTOL aircraft are generally unstable in a significant portion of their flight envelope. Consequently, an active flight control system is required to fly the aircraft or perform simulation studies. Flight control system design for complex eVTOL aircraft is a major challenge for many reasons, including: inherent vehicle instability, strong aerodynamic nonlinearities, interaction effects, and ambiguous control allocation strategies due to the availability of many redundant control effectors. The baseline control framework implemented in the simulation, described in Refs. [28, 29], is referred to as the Robust Uniform Control Approach for vertical takeoff and landing (VTOL) aircraft. The approach integrates a robust servomechanism linear quadratic regulator (RSLQR) control framework with control allocation techniques and airspeed-based gain scheduling to develop a full-envelope flight controller. The controller has been successfully applied to multiple eVTOL aircraft configuration types across their operational flight envelopes [28, 29].

Although atmospheric turbulence models are included within the simulation architecture, for this study, flight simulations were performed in still air, for simplicity. The simulated flight data were corrupted with white, Gaussian measurement noise. The sensor noise levels used for this work emulate those implemented in a simulation-based aircraft system identification study performed in Ref. [30]. Sensor bias and scale factor errors generally seen in flight data were not considered because these systematic instrumentation errors would be removed using kinematic consistency correction techniques prior to model identification [16].

B. LA-8 Aircraft

The Langley Aerodrome No. 8 (LA-8) [6], pictured in Fig. 1, is a subscale, tandem tilt-wing, distributed electric propulsion aircraft configuration intended to be a testbed for eVTOL aircraft technology. The LA-8 was developed at NASA Langley Research Center as one of several eVTOL aircraft concepts intended to explore their unique flight characteristics and resolve implementation challenges to help bring similar full-scale vehicles into mainstream operation. The LA-8 is equipped with 20 control effectors, including two tilting wings, four elevons, four single-slotted Fowler flaps, two ruddervators, and eight fixed-pitch propellers. A diagram of the propulsors and control surface definitions is shown in Fig. 2. Wing, elevon, flap, and ruddervator deflections are defined positive trailing edge downward. Propellers 1, 3, 6, and 8 rotate clockwise and propellers 2, 4, 5, and 7 rotate counterclockwise, as viewed from the rear.

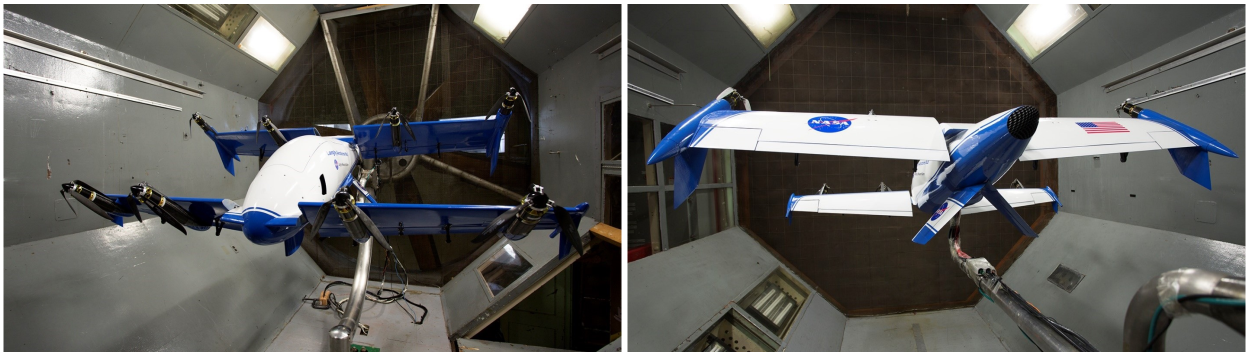

(a) LA-8 front view **(b) LA-8 rear view**

Fig. 1 LA-8 mounted in the NASA Langley 12-Foot Low-Speed Tunnel.

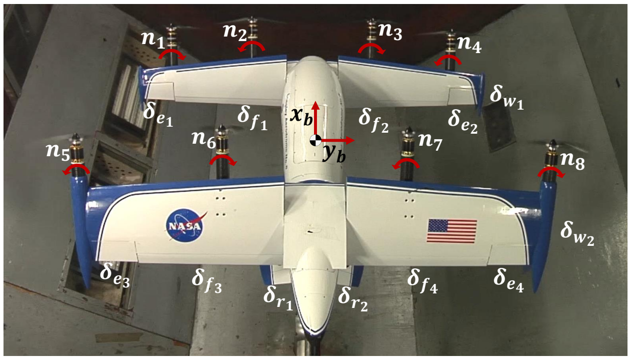

Fig. 2 LA-8 propulsor and control surface definitions.

The LA-8 aero-propulsive model development process using wind tunnel testing is described in Refs. [11, 13, 27, 31]. The aero-propulsive model consists of a set of nonlinear response surface equations describing the aerodynamic and propulsion forces and moments exerted on the aircraft at several discrete reference airspeed conditions throughout the vehicle flight envelope. These point model responses are then blended together to enable continuous simulation from hover through forward flight. Two approaches were used to identify the aero-propulsive response surface equations [11]. The first approach used data from a powered-airframe wind tunnel experiment executed at multiple freestream velocity settings to develop the model. A second approach sought to produce a higher fidelity model utilizing isolated propulsion data in concert with powered-airframe data. The latter, more complex model was used to perform flight simulations for this study. A future report is expected to be published providing LA-8 aero-propulsive models across the operational flight envelope of the vehicle [32].

III. eVTOL Aircraft Modeling Approach

Aero-propulsive modeling for eVTOL aircraft requires a different approach compared to conventional fixed-wing and rotary-wing aircraft modeling approaches. eVTOL vehicles can be considered a fixed-wing/rotary-wing hybrid, suggesting that a combination of the two modeling methodologies will facilitate suitable model development. Accordingly, the modeling approach defined here applies relevant aspects from both fixed-wing and rotary-wing system identification and incorporates strategies specific to eVTOL aircraft. The proposed eVTOL aircraft system identification method focuses on developing a model of the aero-propulsive forces and moments exerted on the aircraft as a function of vehicle state and control variables. The approach is informed by vehicle attributes, as well as experience gained from past eVTOL aircraft model development studies using CFD and wind tunnel testing [8, 11]. Note that the approach in this paper applies when most or all of the distributed propulsors are operational on the aircraft. Certain vehicles, such as the lift+cruise configuration type [1], disable most propulsion elements when operating in a high-speed forward flight condition. For that aircraft type and flight regime, for example, a fixed-wing system identification approach would be applicable, as was used in Ref. [8].

Following the rotorcraft modeling convention, the aero-propulsive models are developed and estimated in a dimensional form. The response variables are defined as the dimensional body-axis applied aero-propulsive forces and moments X, Y, Z, L, M, and N, as opposed to nondimensional aerodynamic force and moment coefficients C_x, C_y, C_z, C_l, C_m, and C_n normalized by freestream dynamic pressure $\bar{q} = \frac{1}{2}\rho V^2$ and aircraft geometry. Nondimensionalization by freestream dynamic pressure is not valid for vehicles that are propulsion-dominated and experience significant airframe-propulsion interaction. Propulsor aerodynamics, for example, scale with the dynamic pressure experienced by the individual propeller blades, as opposed to freestream dynamic pressure. Also, the dimensionless force and moment coefficients would be undefined in hover due to division by zero freestream dynamic pressure. A generally nonlinear multivariate polynomial modeling approach adopted from fixed-wing applications has been used in previous studies to capture the nonlinear aero-propulsive effects [8, 11]. Significant airframe-propulsion interactions and rapid aerodynamic variation with flight condition for eVTOL vehicles suggests that a linear aero-propulsive model will have a small region of local validity. For many applications, identification of a nonlinear aero-propulsive model will be required; however, for this work, a linear aero-propulsive model structure used with the nonlinear aircraft equations of motion was found to produce adequate modeling results for small perturbations from a reference flight condition. For this reason, a linear aero-propulsive model was used as the local model structure and linear model parameters were identified at numerous flight conditions across the LA-8 flight envelope to develop a nominal model for the purpose of illustrating system identification applied to eVTOL aircraft. This approach is similar to previous work that identified and combined linear models to produce a global model [23]. The method used for this paper can be readily extended to using nonlinear aero-propulsive models in future studies.

Although the dimensional forces and moments are defined as the responses to be modeled, these quantities cannot be measured directly in flight and must be inferred from other measurements. The dimensional applied forces are calculated as the vehicle mass multiplied by the body-axis translational accelerometer measurements corrected to the aircraft center of gravity:

$$X = ma_x, \quad Y = ma_y, \quad Z = ma_z \tag{9}$$

The applied moments are calculated using the rotational dynamic equations accounting for propulsor gyroscopic effects [cf. Eqs. (4)-(6)] as:

$$L = I_x \dot{p} - I_{xz} \dot{r} + (I_z - I_y) qr - I_{xz} pq + \dot{h}_x + q h_z - r h_y \tag{10}$$

$$M = I_y \dot{q} + (I_x - I_z) pr + I_{xz} (p^2 - r^2) + \dot{h}_y + r h_x - p h_z \tag{11}$$

$$N = I_z \dot{r} - I_{xz} \dot{p} + (I_y - I_x) pq + I_{xz} qr + \dot{h}_z + p h_y - q h_x \tag{12}$$

It is important to include propulsor gyroscopic effects in these equations because the propulsors will be dynamically commanded and asymmetrically operated during maneuvers used for system identification.

The vehicle states defined as explanatory variables for modeling include the body-axis translational velocity components u, v, w in ft/s and angular velocity components p, q, r in rad/s, following the convention used in rotorcraft system identification. The longitudinal force and moment components $(X,\ Z,\ M)$ use only the longitudinal states (u, w, q) as explanatory variables, and the lateral-directional force and moment components $(Y,\ L,\ N)$ use only the lateral-directional states (v, p, r) as explanatory variables. Formulation in terms of body-axis velocity components, as opposed to airflow angles α and β, allows the state explanatory variables to be defined across the flight envelope, including in hover. The state variables are expressed in their dimensional form for modeling because the forces and moments are also described dimensionally. The vehicle control surface deflection angles in radians are also defined as explanatory variables, as is commonly done for fixed-wing aircraft system identification.

To complete the definition of proposed modeling variables, the rotational speeds of each propulsor in revolutions/s are defined as explanatory variables, which applies for modeling vehicles with fixed-pitch propellers. If the vehicle had variable-pitch propellers, the propulsion explanatory variables for each propulsor would be both rotational speed and blade pitch angle. This formulation deviates from fixed-wing modeling where propulsion aerodynamics are generally not characterized in flight, and rotary-wing aircraft modeling which generally includes more rotor states. Many conventional helicopter rotor states, such as flapping, lead-lag, and coning, are not as relevant to eVTOL vehicles because of smaller and stiffer propeller blades, and measuring or estimating these quantities for each propulsor would be challenging. These additional rotor states are not necessary to capture dominant eVTOL vehicle aerodynamic dependencies due to the smaller diameter, higher rigidity distributed propellers and reduced mechanical complexity compared to articulated rotors. Rotorcraft modeling studies also often include pilot control positions as explanatory variables because rotor collective and cyclic blade pitch angles are difficult to measure. This is not acceptable for modeling eVTOL aircraft because the number of control surfaces and propulsors is greater than the number of pilot inputs.

For this work, the forward airspeed component u is treated as a flight condition variable, where local models are identified at a set of reference airspeed conditions u_o. Density altitude h, or atmospheric density ρ, could be included as another flight condition variable, but the approach taken here is to develop modeling techniques at a single altitude. Additionally, wing tilt angles for the LA-8 vehicle are treated as flight condition variables scheduled with airspeed, as opposed to being defined as explanatory variables. Including wing tilt angles as explanatory variables would introduce additional complications because the propellers, wings, and wing-fixed control surfaces all change orientation with respect to the body-axes. Also, the assumption that the aircraft is operating as a single rigid body would be violated. Treating wing angles as configuration variables assumes an existing wing angle schedule.

The flight condition variables, explanatory variables, and response variables defined for the LA-8 aircraft used in this work are summarized in Table 1. As mentioned above, a fixed linear aero-propulsive model structure was used for developing a local model for each reference flight condition and several linear models were developed throughout the nominal flight envelope. For example, the local model structure for Z is:

$$\begin{aligned} Z = {} & Z_u u + Z_w w + Z_q q + Z_{\delta_{e_1}} \delta_{e_1} + Z_{\delta_{e_2}} \delta_{e_2} + Z_{\delta_{e_3}} \delta_{e_3} + Z_{\delta_{e_4}} \delta_{e_4} + Z_{\delta_{f_1}} \delta_{f_1} + Z_{\delta_{f_2}} \delta_{f_2} + Z_{\delta_{f_3}} \delta_{f_3} + Z_{\delta_{f_4}} \delta_{f_4} + \dots \\ & + Z_{\delta_{r_1}} \delta_{r_1} + Z_{\delta_{r_2}} \delta_{r_2} + Z_{n_1} n_1 + Z_{n_2} n_2 + Z_{n_3} n_3 + Z_{n_4} n_4 + Z_{n_5} n_5 + Z_{n_6} n_6 + Z_{n_7} n_7 + Z_{n_8} n_8 + Z_o \end{aligned} \tag{13}$$

Here, Z_o contains the aerodynamic bias as well as contributions related to the regressor reference values [16]. The model structures for X and M include the same explanatory variables. The model structures for Y, L, and N are similar, with the only difference being that v, p, and r are included as explanatory variables, as opposed to u, w, and q. The next section discusses an experimental design methodology which ensures the effects of all the explanatory variables on the responses can be adequately characterized.

Table 1 Summary of modeling variables for the LA-8 aircraft

Variable Type	Variable Symbol
flight condition variables	$u_o, \delta_{w_1}, \delta_{w_2}, h$
explanatory variables	$u, v, w, p, q, r, \delta_{e_1}, \delta_{e_2}, \delta_{e_3}, \delta_{e_4}, \delta_{f_1}, \delta_{f_2}, \delta_{f_3}, \delta_{f_4}, \delta_{r_1}, \delta_{r_2}, n_1, n_2, n_3, n_4, n_5, n_6, n_7, n_8$
response variables	X, Y, Z, L, M, N

IV. Flight Experiment Design

A flight experiment must be properly executed to generate informative data from which a useful model can be identified using the approach outlined in the previous section. This includes the flight test instrumentation and excitation input design strategies, discussed next.

A. Flight Test Instrumentation

The instrumentation requirements for eVTOL aircraft system identification largely follow what is used for research-quality fixed-wing and rotary-wing aircraft testing [16–18]. The desired measurements for LA-8 include body-axis translational acceleration, body-axis angular rates, Euler orientation angles, air data parameters, control surface deflection angles, wing tilt angles, and propulsor rotational speeds. The inertial navigation system should have the built-in capability to provide reconstructed body-axis velocity components through use of a state estimator, such as an extended Kalman filter. This is important for system identification at low airspeed where air data will likely have low signal-to-noise ratios. A sample eVTOL aircraft system identification measurement list for the LA-8 aircraft is summarized in Table 2. Note that different eVTOL aircraft configurations might require other measurements, such as propulsor blade pitch angle and propulsor tilt angle.

Table 2 Sample eVTOL aircraft system identification measurement list for the LA-8 aircraft

Measurement Name	Notes
body-axis translational acceleration (a_x, a_y, a_z)	
body-axis angular velocity (p, q, r)	
Euler orientation angles (ϕ, θ, ψ)	reconstructed via state estimation
true airspeed (V)	
body-axis velocity (u, v, w)	reconstructed via state estimation
airflow angles (α, β)	
static pressure	used to compute air density and density altitude
ambient temperature	used to compute air density and density altitude
control surface deflection angles	
propulsor rotational speeds	
wing tilt angles	

Additional aircraft configuration data are required prior to flight testing. The vehicle mass and moments of inertia should be accurately measured or estimated for use with the aircraft dynamics equations. The moment of inertia of the rotating portion of each propulsor is also needed to properly account for gyroscopic effects. A preliminary estimate of the aircraft dynamic modes and control bandwidth (particularly propulsion control bandwidth) is useful for excitation input design.

B. Input Design

Orthogonal phase-optimized multisine inputs, described in further detail in Refs. [16, 33–35], are the excitation input type used for this work. A multisine input is defined as a sum of multiple sinusoidal functions with different amplitudes, frequencies, and phase angles, where the frequencies are chosen to encompass the frequency range corresponding to the system dynamics of interest. To make all inputs orthogonal in both the time domain and frequency domain, the multisine signal for each jth control effector is assigned sinusoids with a unique subset of discrete harmonic frequency indices K_j selected from the complete set of available frequency indices, K. The available frequencies are $f_k = k/T,\ k = 1, 2, \ldots, K$, where T is the fundamental period. For m total control effectors, each jth input signal $\boldsymbol{u}_j$ is defined as,

$$\boldsymbol{u}_j = \sum_{k \in K_j} A\sqrt{P_k} \sin\left(\frac{2\pi k \boldsymbol{t}}{T} + \phi_k\right) \qquad j = 1, 2, \ldots, m \tag{14}$$

where A is the signal amplitude, P_k is the kth power fraction, ϕ_k is the kth phase angle defined on the interval $[-\pi, +\pi]$, and $\boldsymbol{t}$ is the time vector containing N discrete points. The relative peak factor RPF, defined as,

$$RPF\left(\boldsymbol{u}_j\right) = \frac{1}{\sqrt{2}} \frac{\left[\max\left(\boldsymbol{u}_j\right) - \min\left(\boldsymbol{u}_j\right)\right] / 2}{\sqrt{\boldsymbol{u}_j^T \boldsymbol{u}_j / N}} \tag{15}$$

is the range of input amplitude divided by the root-mean-square of the signal, referenced to the peak factor for a single frequency sinusoidal signal. A RPF value near one is preferred for system identification to prevent perturbing the system far from the reference flight condition. The relative peak factor for a multisine signal is minimized by optimizing the phase angles using the simplex algorithm because the optimization problem is not convex [33]. Minimizing the RPF by phase-shifting the sinusoidal components of a multisine input does not affect the excitation input energy or the mutual orthogonality of the inputs.

For this study, individual multisine signals were generated for each of the LA-8 control surfaces and propulsors, for a total of 18 different excitation signals. Several harmonic components were assigned to each control surface and propulsor multisine signal, where the overall frequency range was set to between 0.05 Hz and 1.8 Hz in accordance with frequencies where the rigid-body dynamics of interest were expected to manifest. The propulsion harmonic components were focused into lower frequencies below 1.2 Hz to adhere to the lower bandwidth of the propulsors [27]. Six different sets of multisine input frequency components were considered for the experiment by varying the fundamental period T from 30 seconds to 180 seconds in 30-second increments. A larger fundamental period results in a finer frequency resolution, $\Delta f = 1/T$ Hz, which allows assigning more frequency components to each individual multisine signal. The design with the shortest fundamental period ($T = 30$ seconds) had three harmonic components assigned to each propulsor and control surface signal; the design with the longest fundamental period ($T = 180$ seconds) had 16 harmonic components assigned to each propulsor signal and 18 harmonic components assigned to each control surface signal. Since the starting phase angles for each harmonic component are generally chosen randomly in $[-\pi, +\pi]$, a different set of phase angles optimized for minimum RPF is generally obtained each time a multisine signal is designed. Multisine optimization with randomly chosen starting phase angles was performed 30 times for each different set of frequency components and the design with the quickest time to decrease pairwise correlation was selected to compare to signals developed with different fundamental periods. The relative peak factor for the design with the quickest time to decrease pairwise correlation for each fundamental period T is shown in Fig. 3; a similar RPF is obtained for each control effector signal for different values of T, with a slight general decreasing trend in RPF as T increases. The propulsor signals also generally have a lower RPF value compared to the control surface signals.

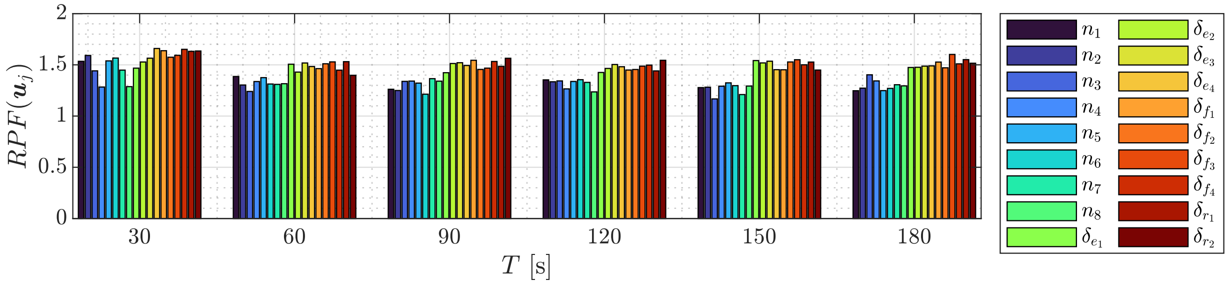

Fig. 3 Relative peak factor of candidate LA-8 aircraft multisine designs.

Multisine signals are orthogonal in the time-domain at integer multiples of T, which might be interpreted to suggest using a multisine design with a small fundamental period. However, obtaining high quality modeling results requires low correlation rather than zero correlation [35], meaning that good modeling results can be obtained by using a maneuver time shorter than the fundamental period of the multisine signal. Also, using a larger number of frequency components provides more diverse dynamic information, which has been shown to improve modeling results [36]. Following an approach similar to Ref. [35], input correlation metrics were used as criteria to assess the quality of each multisine design as maneuver time progresses.

Correlation between two inputs can be assessed using the pairwise correlation coefficient. The correlation coefficient r_{ij} between two input signals, $\boldsymbol{u}_i$ and $\boldsymbol{u}_j$, is defined as,

$$r_{ij} = \frac{(\boldsymbol{u}_i - \bar{u}_i)^T (\boldsymbol{u}_j - \bar{u}_j)}{\sqrt{(\boldsymbol{u}_i - \bar{u}_i)^T (\boldsymbol{u}_i - \bar{u}_i)}\sqrt{(\boldsymbol{u}_j - \bar{u}_j)^T (\boldsymbol{u}_j - \bar{u}_j)}} \tag{16}$$

where $\bar{u}_i$ and $\bar{u}_j$ are the respective mean input signal values. A correlation coefficient value of zero means the signals are uncorrelated, or orthogonal, and an absolute correlation coefficient of one indicates that the signals are completely correlated, or linearly dependent. Lower absolute correlation generally results in better modeling results [35]. A correlation coefficient between signals used for modeling with magnitude greater than 0.9 indicates that data collinearity, or correlation between signals high enough to cause corrupted model identification, may be encountered [16, 17]. The correlation coefficient only quantifies correlation between pairs of inputs, and thus cannot diagnose collinearity among more than two input signals.

An alternative method that can be used to assess multiple correlation between more than two inputs is analysis of the eigenvalues of $\boldsymbol{U}^T\boldsymbol{U}$, where $\boldsymbol{U}$ is a matrix composed of column vectors of the input signals, $\boldsymbol{U} = [\boldsymbol{u}_1, \boldsymbol{u}_2, ..., \boldsymbol{u}_m]$. Assuming that a model includes all input signals, the inverse of the $\boldsymbol{U}^T\boldsymbol{U}$ matrix would be required to compute the ordinary least-squares regression solution. The ratio of the maximum eigenvalue and minimum eigenvalue, $\kappa = \lambda_{\max}/\lambda_{\min}$, is the condition number of the $\boldsymbol{U}^T\boldsymbol{U}$ matrix. A value of κ close to one indicates low multiple correlation whereas a large value of κ indicates an ill-conditioned estimation problem due to data collinearity. Values of κ indicating adverse effects from data collinearity range anywhere from 100 to 100,000 depending on the particular data set [16, 17, 37, 38].

The evolution of correlation metrics over time for each multisine design with a different fundamental period is shown in Fig. 4. Figure 4a shows the maximum absolute pairwise correlation value $|r_{ij}|_{\max}$ for each multisine design as a function of time, with Fig. 4b displaying the same plot over a shorter time interval. Figures 4a-4b show that the pairwise correlation values are zero at integer multiples of the fundamental period of the respective multisine design. The

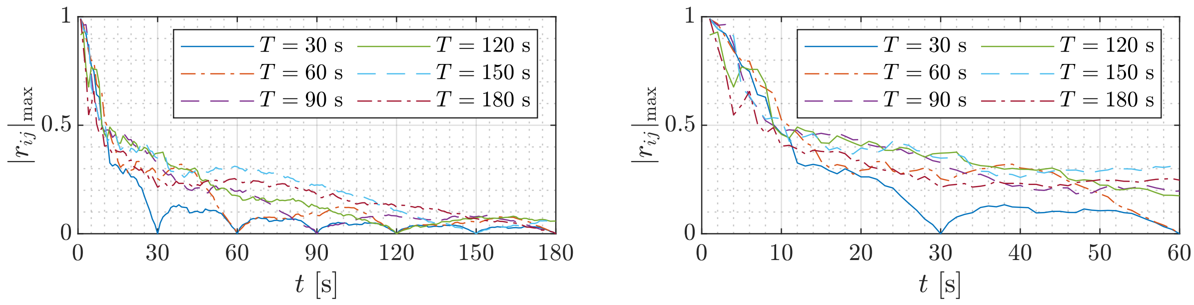

(a) Maximum pairwise correlation coefficient (180 seconds) **(b) Maximum pairwise correlation coefficient (60 seconds)**

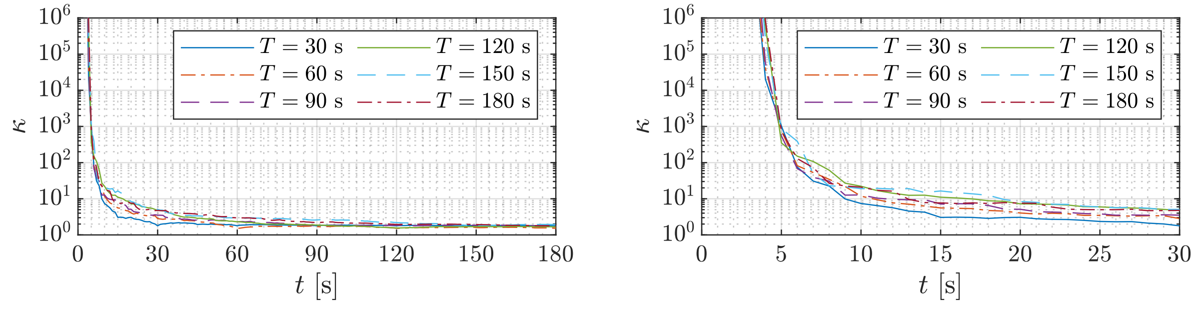

(c) Condition number of $\boldsymbol{U}^T\boldsymbol{U}$ (180 seconds) **(d) Condition number of $\boldsymbol{U}^T\boldsymbol{U}$ (30 seconds)**

Fig. 4 Input signal correlation metrics against time.

maximum correlation for each different multisine design shows a similar rate to decrease below 0.5, which is achieved in roughly 10 seconds. It can also be seen that the design with the greatest fundamental period ($T = 180$ seconds) generally has the lowest maximum pairwise correlation for the first 10 seconds. After 10 seconds, each design has reasonably close $|r_{ij}|_{\max}$ values until approaching the fundamental period for each design, where the signals converge to zero correlation. Figure 4c shows the condition number κ of $\boldsymbol{U}^T\boldsymbol{U}$ for each multisine design as a function of time, with Fig. 4d displaying the same plot over a shorter time interval. All multisine designs achieve a condition number less than 100 in approximately 7 seconds at nearly the same rate and, thereafter, the condition numbers continue to decrease at a slower rate. The overall takeaway from Fig. 4 is that multisine designs with different fundamental periods obtain low correlation metrics in a similar maneuver time. Informed by these time-dependent correlation analysis results and previous research showing the benefits of increased frequency resolution [36], the multisine design with the largest fundamental period ($T = 180$ seconds) was selected to be used for the system identification experiments.

The input spectra for the final set of orthogonal phase-optimized multisine signals with a fundamental period of $T = 180$ seconds is shown in Fig. 5. There are 308 total harmonic components, with 16 frequencies assigned to each propulsor and 18 frequencies assigned to each control surface in an alternating manner. The overall frequency range is between $f_{\min} = 0.05$ Hz and $f_{\max} = 1.756$ Hz with a frequency resolution of $\Delta f = 1/T = 0.00556$ Hz. The input spectra plot shows that the propulsor harmonic components are focused into a lower frequency range, reflecting that the input excitations were designed to be within the bandwidth of the propulsion system. Figure 6 shows the first 20 seconds of the input excitation signals normalized to have a maximum absolute value of one. This reflects how the signals are injected into the flight controller, where a gain is applied to scale each input signal to a sufficient amplitude to obtain a good signal-to-noise ratio, while not deviating far from the trimmed flight condition or perturbing the aircraft to an unsafe flight condition.

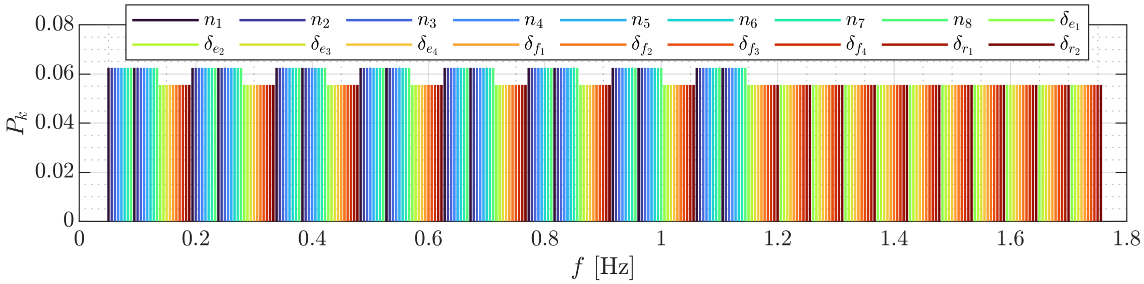

Fig. 5 LA-8 aircraft multisine input spectra for each control effector.

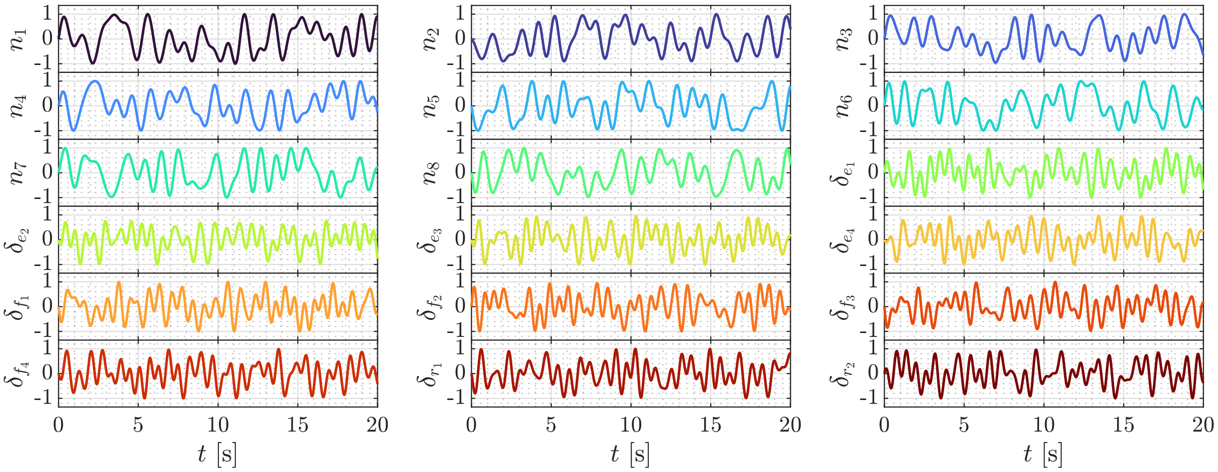

Fig. 6 LA-8 aircraft normalized multisine inputs used for system identification.

C. Input Strategy with Feedback Control

eVTOL aircraft dynamics are generally unstable over a large portion of their flight envelopes, which requires the feedback control system to be active when operating at these conditions. Although necessary for safety, flight control systems can create deficiencies in the data information content available for system identification. Control systems act to suppress the natural aircraft motions that system identification maneuvers are designed to excite, distort optimally designed control inputs, and lead to correlation between explanatory variables, making their independent effects more difficult to distinguish. Strategies used for modeling aircraft with feedback control include using *a priori* information to better condition the modeling problem, lowering the feedback gains, and/or injecting the input excitations downstream of the control laws. Using preliminary information can result in biased estimates if the parameters are not a good representation for actual aircraft characteristics. Also, tampering with the control system is generally not advisable from a risk-mitigation standpoint, particularly for unstable aircraft. Hence, the strategy used here for handling the presence of the flight controller is to sum each input excitation signal with the control effector command from the control system just before the commanded actuator position and rate limits [16]. This approach allows characterizing the influence of each control effector on the aircraft open-loop dynamic response simultaneously. This input excitation framework is depicted in Fig. 7.

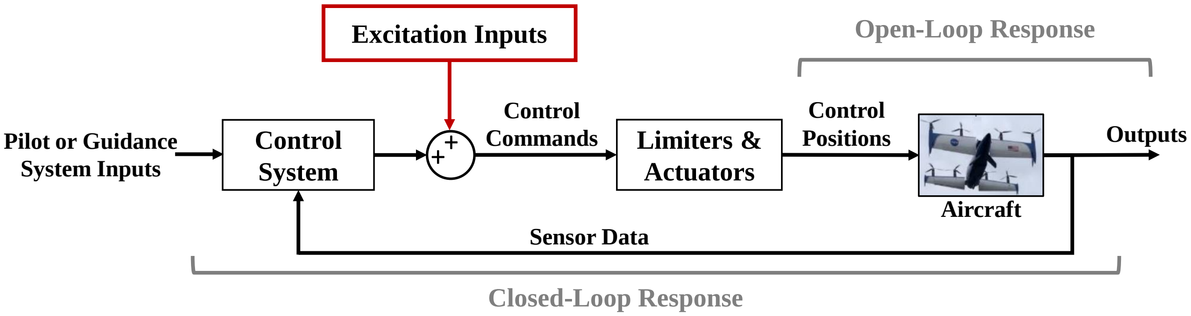

Fig. 7 Proper application of excitation inputs relative to the control system [16].

V. Parameter Estimation

Parameter estimation for this study was performed using the equation-error method formulated in the frequency domain [16, 39, 40]. First, the regressor and response data are detrended and transformed into the frequency domain using a Fourier transform technique leveraging time-domain cubic interpolation and the chirp-z transform to produce a high accuracy transform with an arbitrary frequency range and resolution [16, 41]. The transform frequencies are selected to encompass the aircraft dynamics. This approach effectively smooths the modeling data and allows estimation of nearly unbiased parameter estimates when the regressors contain noise [40, 42]. For this study, the frequency range was selected to match the excitation input design with a fundamental period of $T = 180$ s (see Sec. IV.B); the Fourier transform frequencies were set between $f_{\min} = 0.05$ Hz and $f_{\max} = 1.756$ Hz with a frequency resolution of $\Delta f = 0.00556$ Hz, resulting in $M = 308$ transform frequencies. A parameter sensitivity study indicated that a coarser frequency resolution resulted in parameter estimation errors, whereas a finer frequency resolution provided minimal additional parameter estimation accuracy.

After the modeling data are transformed into the frequency domain, ordinary least-squares regression is applied using the complex regressor and response data. Ordinary least-squares regression is used to estimate a vector of n_p unknown model parameters in a vector $\boldsymbol{\theta}$ for a given model $\tilde{\boldsymbol{y}} = \tilde{\boldsymbol{X}}\boldsymbol{\theta}$ [16]. Here, $\tilde{\boldsymbol{y}}$ is the length M complex model response vector and $\tilde{\boldsymbol{X}}$ is a $M \times n_p$ matrix consisting of column vectors of the complex regressors assumed to be error-free. The regression equation, including the complex measured response variable $\tilde{\boldsymbol{z}}$ corrupted by constant variance, zero-mean, and uncorrelated complex measurement error $\tilde{\boldsymbol{v}}$, is given as:

$$\tilde{\boldsymbol{z}} = \tilde{\boldsymbol{X}}\boldsymbol{\theta} + \tilde{\boldsymbol{v}} \tag{17}$$

For complex least-squares parameter estimation, the optimal estimate of the unknown parameters $\boldsymbol{\theta}$ is determined by minimizing the cost function:

$$J(\boldsymbol{\theta}) = \frac{1}{2}\left(\tilde{\boldsymbol{z}} - \tilde{\boldsymbol{X}}\boldsymbol{\theta}\right)^{\dagger}\left(\tilde{\boldsymbol{z}} - \tilde{\boldsymbol{X}}\boldsymbol{\theta}\right) \tag{18}$$

It follows that the solution to compute an optimal estimate of the unknown real-valued parameters is,

$$\hat{\boldsymbol{\theta}} = \left[Re\left(\tilde{\boldsymbol{X}}^{\dagger}\tilde{\boldsymbol{X}}\right)\right]^{-1} Re\left(\tilde{\boldsymbol{X}}^{\dagger}\tilde{\boldsymbol{z}}\right) \tag{19}$$

where $\hat{\boldsymbol{\theta}}$ is a vector of n_p estimated parameters. The modeled response variable vector is:

$$\hat{\tilde{\boldsymbol{y}}} = \tilde{\boldsymbol{X}}\hat{\boldsymbol{\theta}} \tag{20}$$

A length n_p vector of standard errors $\boldsymbol{s}(\hat{\boldsymbol{\theta}})$ corresponding to the estimated parameters $\hat{\boldsymbol{\theta}}$ is given as:

$$\boldsymbol{s}(\hat{\boldsymbol{\theta}}) = \sqrt{\left(\frac{1}{2T\left(f_{\max} - f_{\min}\right)} Re\left[\left(\tilde{\boldsymbol{z}} - \hat{\tilde{\boldsymbol{y}}}\right)^{\dagger}\left(\tilde{\boldsymbol{z}} - \hat{\tilde{\boldsymbol{y}}}\right)\right]\right)\ \mathrm{diag}\left(\left[Re\left(\tilde{\boldsymbol{X}}^{\dagger}\tilde{\boldsymbol{X}}\right)\right]^{-1}\right)} \tag{21}$$

This form of $\boldsymbol{s}(\hat{\boldsymbol{\theta}})$ accounts for the fact that a frequency range narrower than zero to the Nyquist frequency is used for analysis [40].

After complex least-squares parameter estimation is completed, an additional step is needed to identify the bias term in a model equation [e.g., Z_o in Eq. (13)] because the detrended data used to fit the model parameters contain only dynamic information [16, 40]. The bias parameter estimate $\hat{\theta}_o$ is estimated as the mean value of $(\boldsymbol{z} - \boldsymbol{X}\hat{\boldsymbol{\theta}})$, where $\boldsymbol{z}$ is the measured response variable in the time domain, $\boldsymbol{X}$ is a matrix consisting of column vectors of the regressors in the time domain, and $\hat{\boldsymbol{\theta}}$ is the model parameter vector estimated previously using complex least-squares regression.

VI. Results

As described in Sec. III, the modeling approach used for this paper is to identify several linear aero-propulsive models across the nominal flight envelope for the LA-8 aircraft. The local model parameters are then blended together to form a global aero-propulsive model. Sample local and global modeling results obtained from simulated LA-8 flight tests are provided in this section.

A. Local Modeling Results

Simulated LA-8 flight data for a level maneuver at a reference forward airspeed of u_o = 45 ft/s and wing angles fixed at $\delta_{w_1} = \delta_{w_2} = 25$ deg with orthogonal phase-optimized multisine inputs active on all control surfaces and propulsors are shown in Figs. 8-9. As mentioned previously, the simulated flight data used for modeling were corrupted with measurement error using noise levels consistent with a previous simulation-based aircraft system identification study [30]. The control effector signal waveform shown in Fig. 8 is different than the designed signals shown in Fig. 6 due to distortion from the active flight control system. Even with this distortion, modeling variables are still sufficiently decorrelated for model identification as a result of injecting the excitation inputs as shown in Fig. 7 [16]. A total maneuver length of 60 seconds was selected by investigating the parameter estimation results and the root-mean-square error (RMSE) for validation data as a function of maneuver time used for modeling, as will be demonstrated below. All of the following analysis in this subsection uses the simulated flight data shown in Figs. 8-9, where the first 40 seconds are used for model identification and the last 20 seconds are used for model validation.

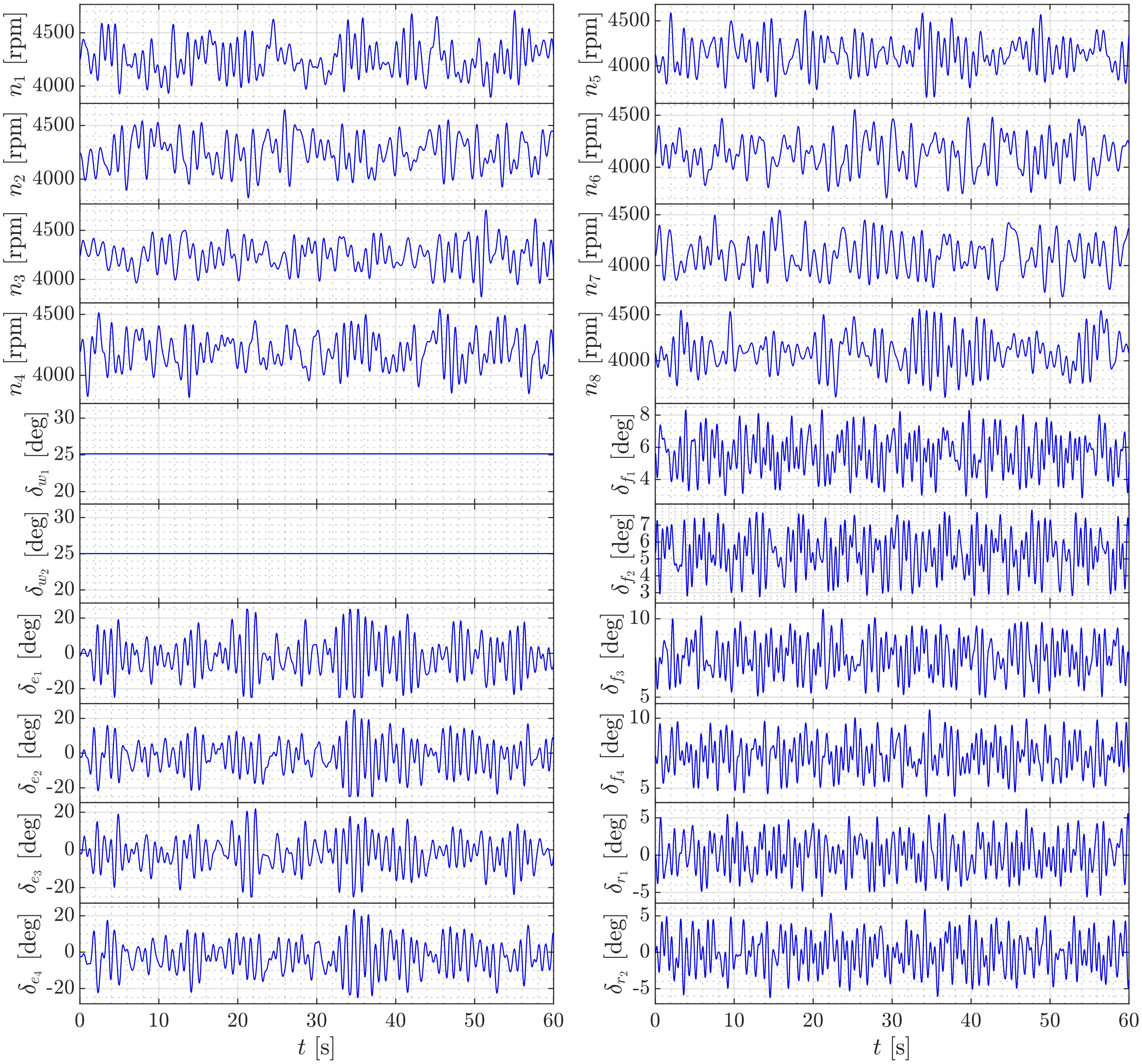

Fig. 8 Control surface deflection angles and propulsor rotational speeds during a simulated LA-8 system identification maneuver at u_o = 45 ft/s.

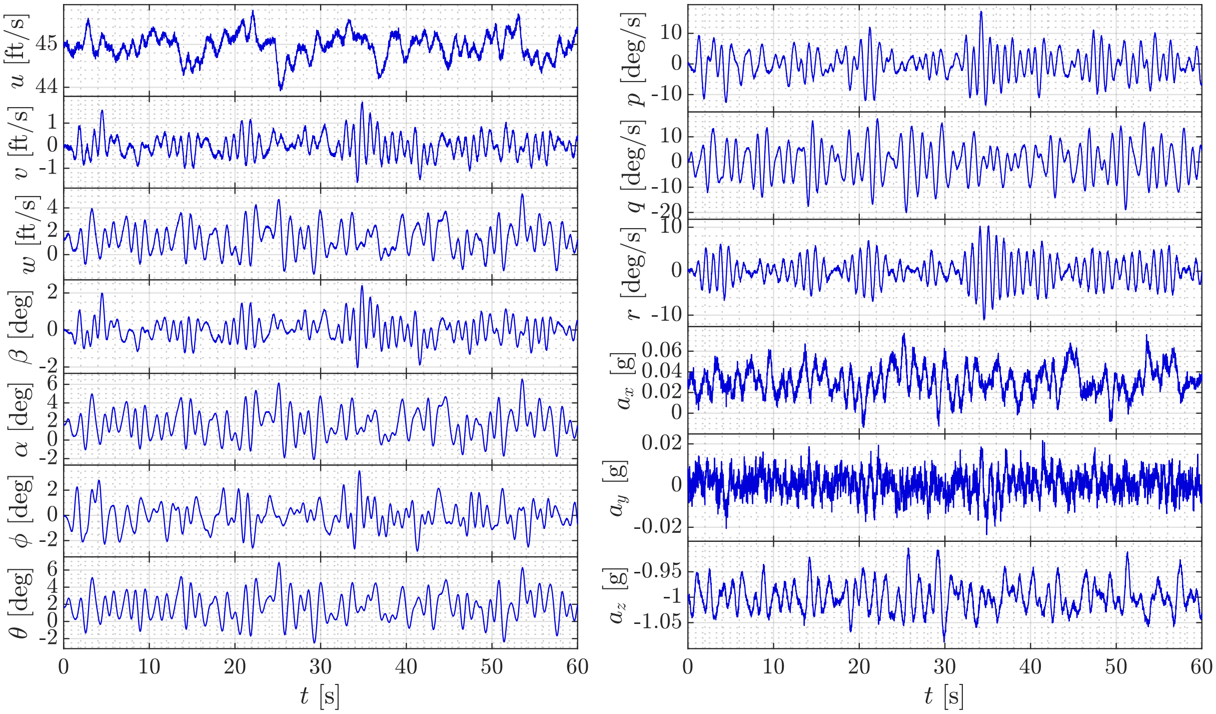

Fig. 9 Simulated LA-8 flight data at u_o = 45 ft/s with multisine inputs active on all control effectors.

Figure 10 shows the Z parameter estimates and error bars of $\pm 2s(\hat{\boldsymbol{\theta}})$ computed using complex least-squares regression against the amount of maneuver time used for modeling. Parameter estimates were computed in a batch manner for the various different maneuver lengths used for modeling, as opposed to implementing real-time calculations. The plot also shows the linearized parameters computed directly from the nonlinear LA-8 simulation using central finite differences, for comparison. The parameters appear to converge to reasonably consistent values by the time 40 seconds has elapsed and show good concurrence with the linearized LA-8 simulation parameters. Similar results were obtained for the parameters corresponding to the other aero-propulsive forces and moments and at different flight conditions throughout the LA-8 flight envelope. Note that the parameter estimates contain asymmetries that are not apparent from the LA-8 vehicle configuration. This is a result of manufacturing differences between the clockwise and counterclockwise propellers, which resulted in a significant difference in thrust production between the propeller variants [31]. Since the propulsion-only and propulsion-airframe interaction effects are significant, this propulsion asymmetry is manifested in many model terms [11].

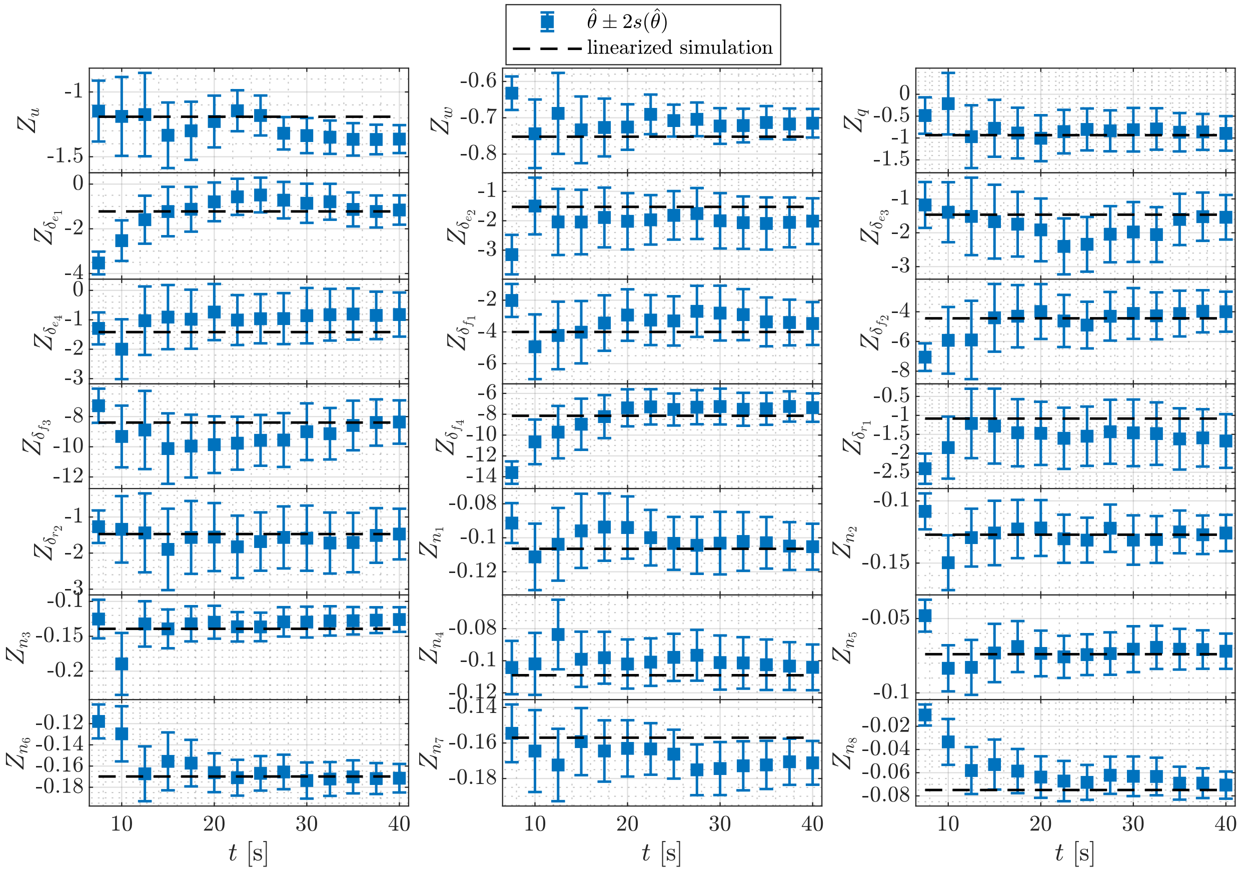

Fig. 10 Variation of Z parameter estimates with maneuver time used for modeling at u_o = 45 ft/s.

Figure 11 shows the validation RMSE (RMSE$_v$) in the time domain for each response variable against the amount of maneuver time used for modeling. RMSE is calculated as,

$$\text{RMSE} = \sqrt{\frac{(z - \hat{y})^T\ (z - \hat{y})}{N}} \tag{22}$$

where $\hat{y}$ is the length N model response vector and z is the length N measured response vector. The last 20 seconds of data from the maneuver shown in Figs. 8-9 were used to compute the RMSE$_v$ metric at each modeling time length. The amount of time for RMSE$_v$ to nearly level off is different for each response, but all responses appear to have a small RSME$_v$ reduction rate by the time 40 seconds has elapsed, indicating that a longer maneuver would provide little additional benefit. Similar results were obtained at other flight conditions.

In view of Figs. 10-11, and also with the knowledge that 40 seconds is the amount of time needed to complete two full periods of the lowest frequency sinusoidal component of the multisine maneuver ($f_{\min}$ = 0.05 Hz), 40 seconds was selected as the amount of maneuver time to use for modeling at each flight condition. A 60 second maneuver was executed at each reference flight condition used for model identification, where the first 40 seconds were used to identify the local aero-propulsive model, and the last 20 seconds of the maneuver were used as validation data to test the model prediction capability. This maneuver time length worked well across the LA-8 flight envelope, as will be shown in Sec. VI.B.

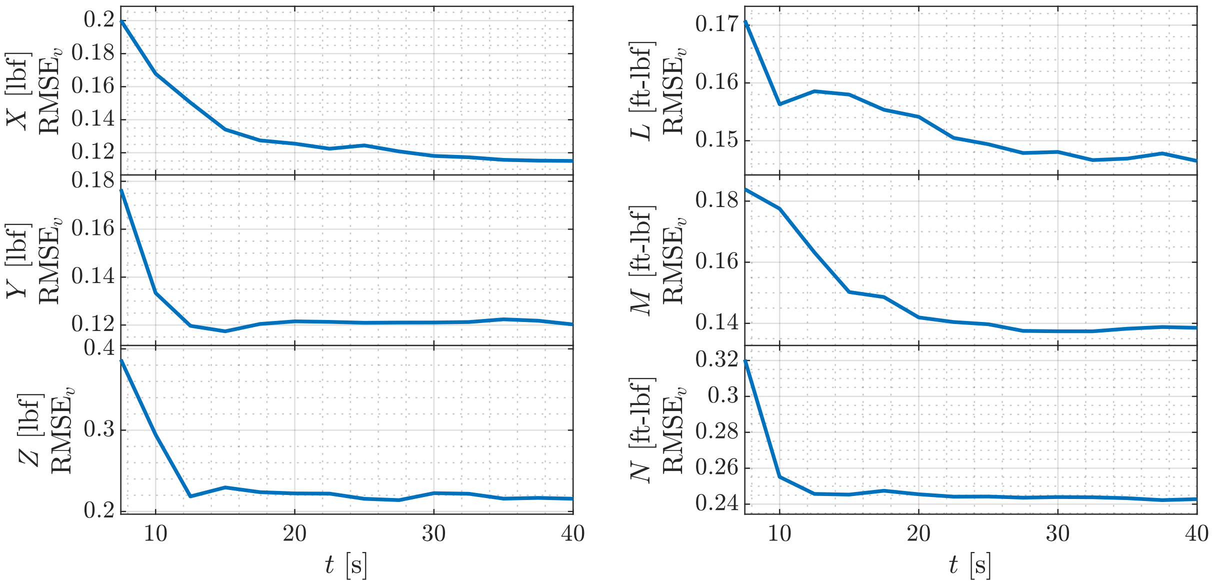

Fig. 11 Variation of validation RMSE with maneuver time used for modeling at u_o = 45 ft/s.

Figure 12 shows the model fit in the frequency domain using the first 40 seconds of the maneuver shown in Figs. 8-9. A good model fit is observed for each response. The coefficient of determination (R^2) metric shown on the plot for each response is high, indicating that most of the variation of the response variable about its mean is characterized by the model. Figure 13 shows the model fit and model prediction compared to the smoothed aero-propulsive forces and moments in the time domain using the same maneuver. The model fit and model predictions are close to the responses calculated from the simulated flight data, indicating that the model is able to describe a large amount of the variation in each response. The local model fit and prediction capability were similar for the other reference flight conditions across the LA-8 flight envelope.

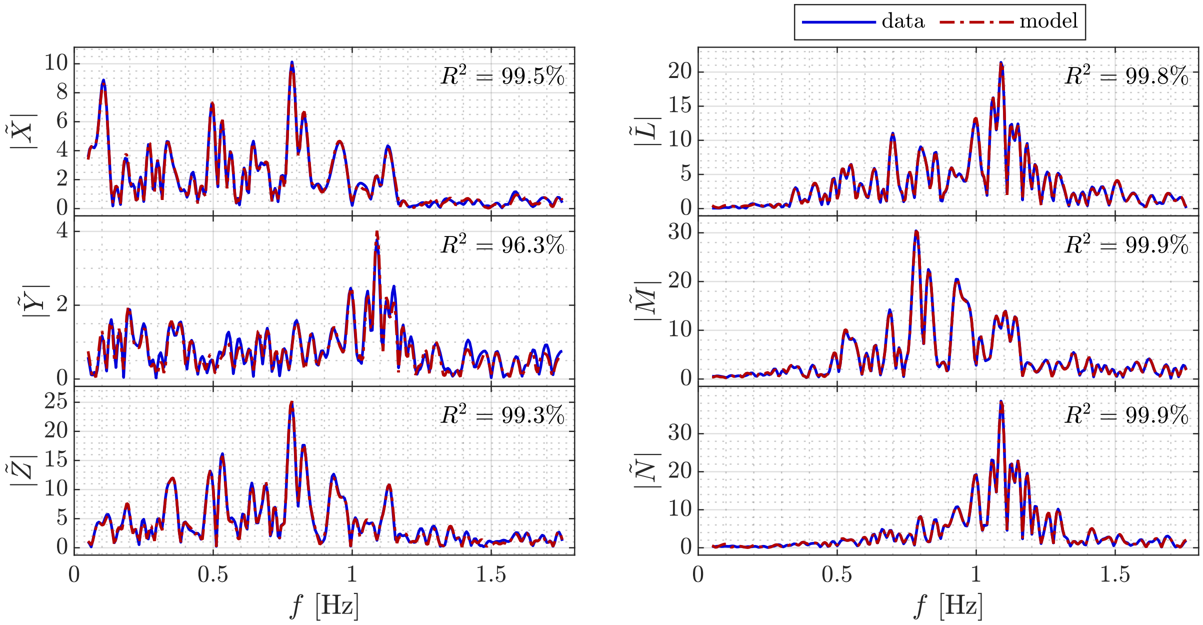

Fig. 12 Comparison of modeling response data and model fit in the frequency domain at u_o = 45 ft/s.

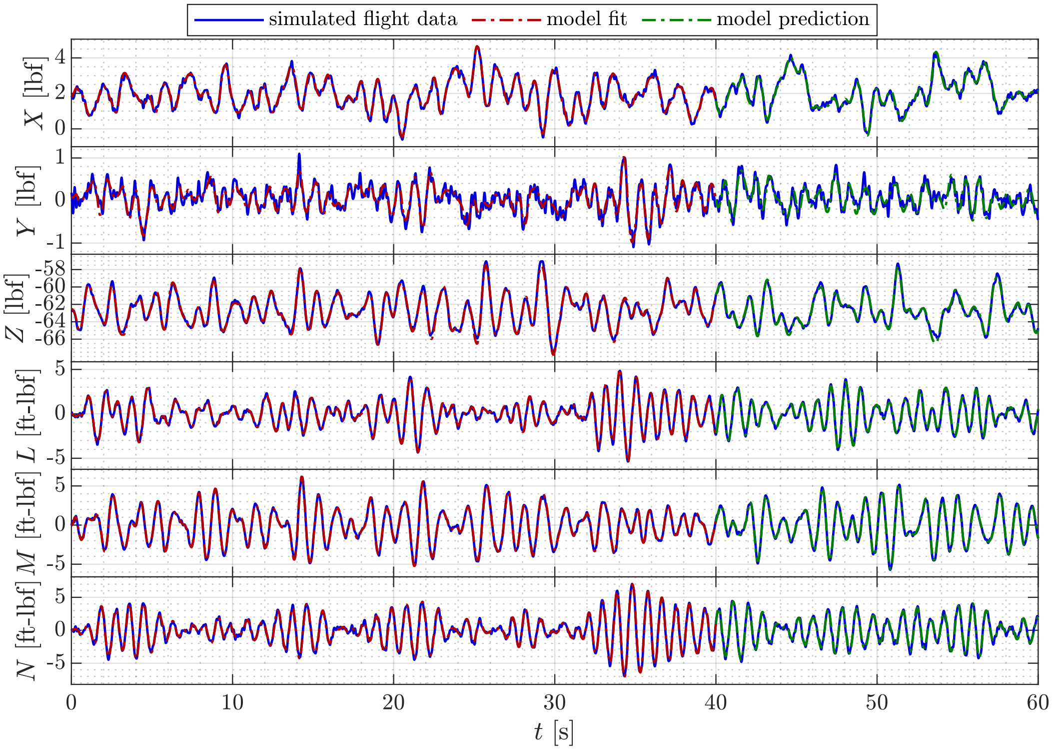

Fig. 13 Model fit and model prediction in the time domain for a simulated LA-8 maneuver at u_o = 45 ft/s.

B. Global Modeling Results

Similar execution of a 60-second multisine maneuver and the subsequent analysis shown in the previous subsection were used to develop a local model at several flight conditions throughout the LA-8 flight envelope. The model fit and model predictions in the time domain for seven different flight conditions through the LA-8 transition envelope are shown in Fig. 14. A good model fit and good model predictions are observed for each flight condition. Figure 15 shows the RMSE value for each response for both modeling data and validation data. Observing that the modeling RMSE for each response holds a similar value to the corresponding validation RMSE, the modeling RMSE values are an accurate representation of prediction performance suggesting that modeling was successful.

Although maneuvering between flight conditions is not shown in Fig. 14, the plots still reflect how a practical flight test for the LA-8 aircraft would occur. The testing would start in a hover flight condition to develop an initial model and then testing would move gradually through transition to eventually develop models through the nominal flight envelope. This could occur in a single flight, could involve the aircraft returning to the ground between test points, or could be some combination of the two strategies. This approach would work well alongside safe envelope expansion flight testing and could be used to aid in tuning a flight controller to achieve a safe transition. Note that the forward airspeed conditions tested for this study ranged from 0 to 54 ft/s and the wing angles ranged from approximately 83 deg (the trimmed hover setting) to 15 deg. For an actual system identification flight test of the LA-8 vehicle, modeling would be performed through wing angles of 0 deg (forward flight); however, for this simulated study, the possible flight conditions were limited by the range of validity of the wind tunnel derived aero-propulsive models currently implemented in the LA-8 simulation.

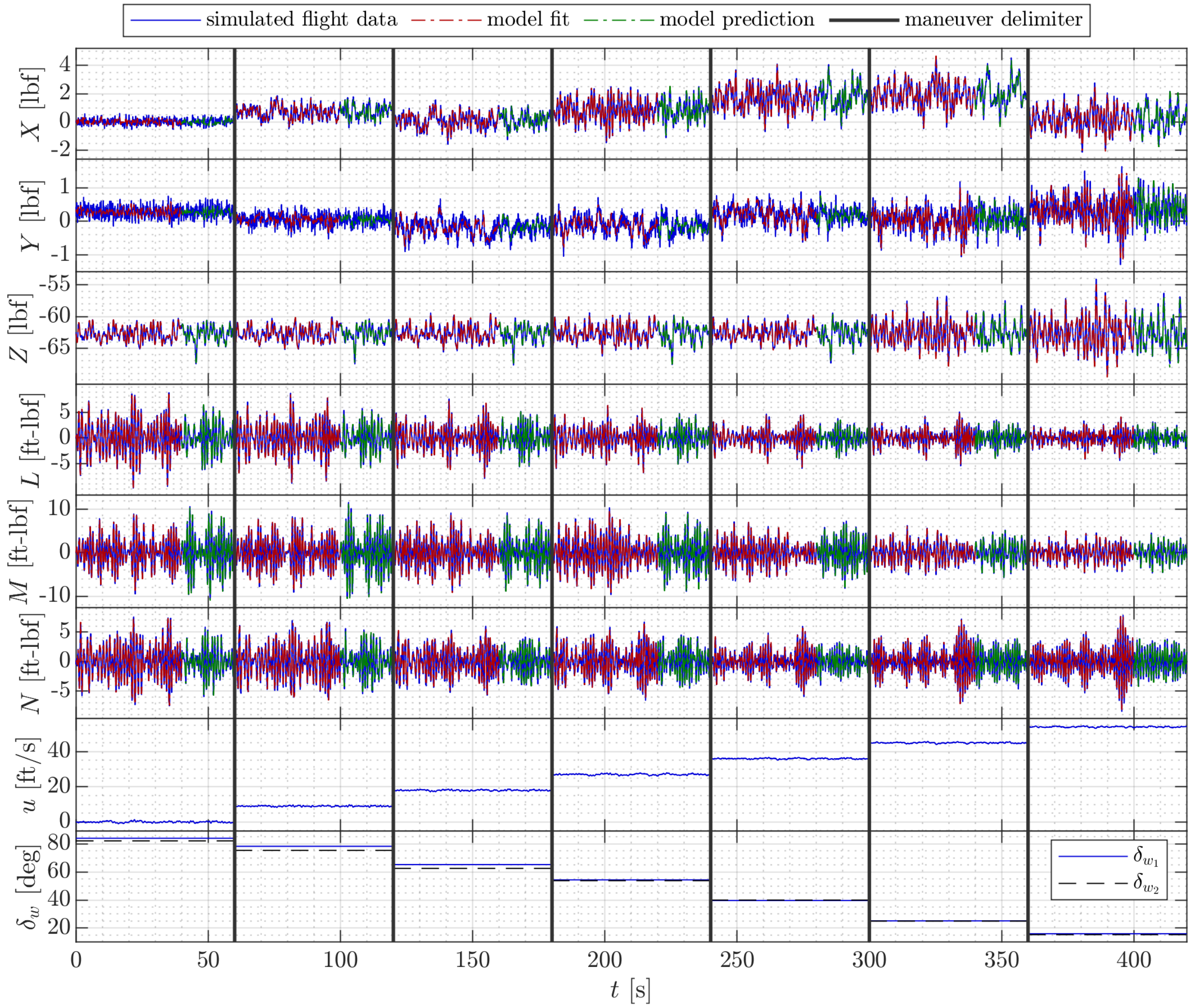

Fig. 14 Model fit and model prediction for the aero-propulsive forces and moments at several reference conditions throughout the LA-8 transition envelope.

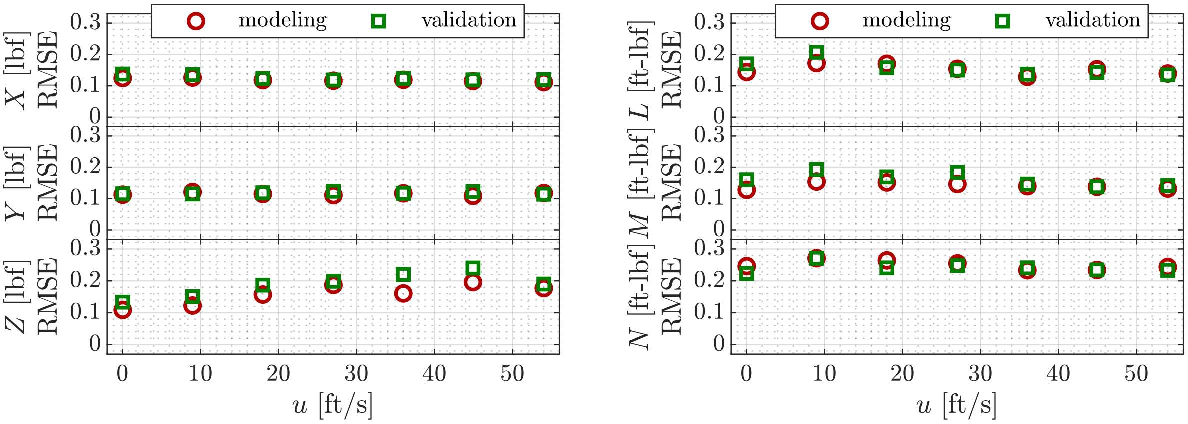

Fig. 15 Modeling and validation RMSE for each response against reference forward speed.

Figure 16 shows the Z parameter estimates and error bars of $\pm 2s(\hat{\boldsymbol{\theta}})$ computed using complex least-squares regression for each tested flight condition. The solid line connecting the parameters is computed using shape-preserving piecewise cubic interpolation [43, 44] with the `pchip.m` MATLAB® function[‡]; this interpolation method is preferred over cubic spline interpolation for blending parameter estimates because of its tendency to avoid overshoot and oscillatory behavior. Blending local model parameter estimates using this method shows how a continuous simulation can be formed using local models identified at several different reference conditions. The linearized parameters computed directly from the nonlinear LA-8 simulation at each condition are also shown for comparison. The identified Z parameters show good concurrence with the linearized LA-8 simulation parameters across the flight envelope. Similar results were obtained for the parameters corresponding to the other aero-propulsive forces and moments.

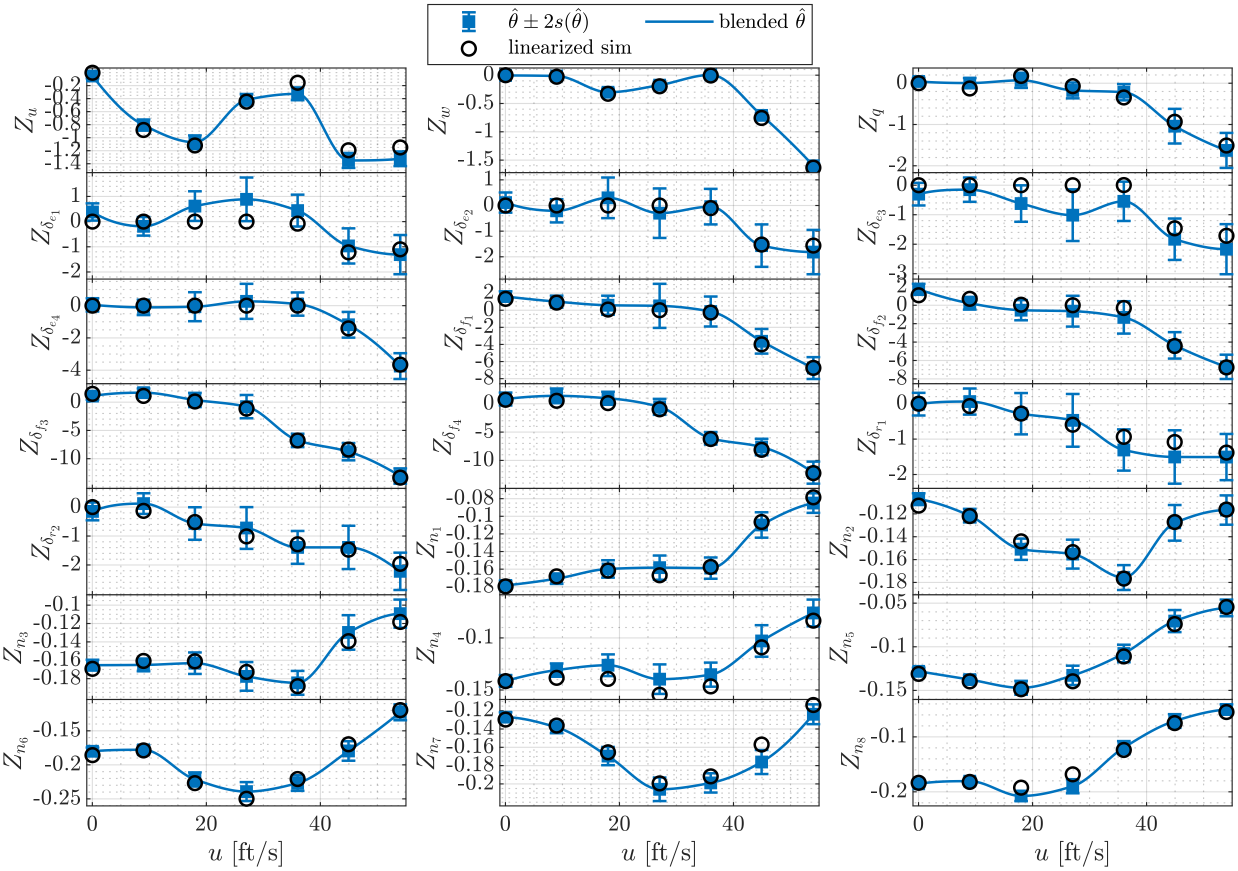

Fig. 16 Variation of Z parameter estimates with forward speed across the LA-8 flight envelope.

VII. Conclusions

eVTOL vehicles are a new type of aircraft exhibiting aerodynamic characteristics of both fixed-wing and rotary-wing aircraft as well as challenging vehicle-specific attributes, such as many available control effectors to characterize. The aircraft are also generally unstable and have a wide range of operational flight conditions. This paper developed a system identification methodology for eVTOL aircraft leveraging system identification techniques for fixed-wing and rotary-wing aircraft, as well as previous eVTOL aircraft aero-propulsive characterization studies. The proposed method was evaluated using a high-fidelity flight dynamics simulation for the LA-8 tandem tilt-wing eVTOL aircraft.

An experimental design for the LA-8 was developed using orthogonal phase-optimized multisine signals designed for each individual control surface and propulsor. Several multisine designs were compared varying the fundamental period, which indicated that maneuvers with a longer fundamental period would be beneficial for model identification.

[‡] Information available online at https://www.mathworks.com/help/matlab/ref/pchip.html [retrieved 12 October 2021].

Since the aircraft is unstable, system identification maneuvers were executed with the flight control system active, but the strategy still effectively excited the LA-8 aircraft dynamics allowing accurate modeling throughout the flight envelope. A 40 second modeling maneuver was shown to be an adequate length for accurate local model identification for the investigated vehicle and demonstrates the utility of using multiple-input orthogonal optimized multisine maneuvers for efficient eVTOL aircraft system identification.

Model parameters in a linear aero-propulsive model structure used with the nonlinear aircraft equations of motion were estimated at several different flight conditions throughout the LA-8 flight envelope. Parameter estimation was performed using the equation-error method in the frequency domain. The model structure is appropriate for capturing eVTOL aircraft characteristics in small perturbation maneuvers from a trimmed flight condition; however, the approach can also be readily extended to develop nonlinear aero-propulsive models that increase the region of model validity. The identified models were shown to have good predictive capability, small model fit error, and good agreement with linearized simulation parameters. A blending method was shown which allows development of a global aero-propulsive model through the nominal flight envelope of the vehicle. Model development flight testing strategies were discussed allowing safe envelope expansion and sequential flight controller tuning for a new vehicle.

This work provides progress in eVTOL aircraft modeling research using flight test techniques that can be applied for many current and future vehicles. The general method will allow accurate identification of a dynamic model for complex, unstable eVTOL aircraft configurations using a short amount of flight test time and with minimal additional risk posed to the vehicle. Future system identification studies are anticipated to further refine aero-propulsive model development methodologies.

Acknowledgments

This research was funded by the NASA Aeronautics Research Mission Directorate (ARMD) Transformational Tools and Technologies (TTT) project. Jacob Cook developed the LA-8 aircraft flight controller and integrated the controller into the simulation used for this work. Vehicle simulation development support was provided by Thomas Britton. Conversations about this work with Eugene Morelli are acknowledged and greatly appreciated.

References

[1] Silva, C., Johnson, W., Antcliff, K. R., and Patterson, M. D., "VTOL Urban Air Mobility Concept Vehicles for Technology Development," *2018 Aviation Technology, Integration, and Operations Conference*, AIAA Paper 2018-3847, Jun. 2018. https://doi.org/10.2514/6.2018-3847.

[2] Johnson, W., Silva, C., and Solis, E., "Concept Vehicles for VTOL Air Taxi Operations," *AHS Technical Conference on Aeromechanics Design for Transformative Vertical Flight*, Jan. 2018.

[3] Saeed, A. S., Younes, A. B., Cai, C., and Cai, G., "A survey of hybrid Unmanned Aerial Vehicles," *Progress in Aerospace Sciences*, Vol. 98, 2018, pp. 91–105. https://doi.org/10.1016/j.paerosci.2018.03.007.

[4] Kim, H. D., Perry, A. T., and Ansell, P. J., "A Review of Distributed Electric Propulsion Concepts for Air Vehicle Technology," *2018 AIAA/IEEE Electric Aircraft Technologies Symposium*, AIAA Paper 2018-4998, Jul. 2018. https://doi.org/10.2514/6.2018-4998.

[5] Rothhaar, P. M., Murphy, P. C., Bacon, B. J., Gregory, I. M., Grauer, J. A., Busan, R. C., and Croom, M. A., "NASA Langley Distributed Propulsion VTOL Tilt-Wing Aircraft Testing, Modeling, Simulation, Control, and Flight Test Development," *14th AIAA Aviation Technology, Integration, and Operations Conference*, AIAA Paper 2014-2999, Jun. 2014. https://doi.org/10.2514/6.2014-2999.

[6] North, D. D., Howland, G., and Busan, R. C., "Design and Fabrication of the Langley Aerodrome No. 8 Distributed Electric Propulsion VTOL Testbed," *AIAA SciTech 2021 Forum*, AIAA Paper 2021-1188, Jan. 2021. https://doi.org/10.2514/6.2021-1188.

[7] Murphy, P. C., Buning, P. G., and Simmons, B. M., "Rapid Aero Modeling for Urban Air Mobility Aircraft in Computational Experiments," *AIAA SciTech 2021 Forum*, AIAA Paper 2021-1002, Jan. 2021. https://doi.org/10.2514/6.2021-1002.

[8] Simmons, B. M., Buning, P. G., and Murphy, P. C., "Full-Envelope Aero-Propulsive Model Identification for Lift+Cruise Aircraft Using Computational Experiments," *AIAA AVIATION 2021 Forum*, AIAA Paper 2021-3170, Aug. 2021. https://doi.org/10.2514/6.2021-3170.

[9] Busan, R. C., Rothhaar, P. M., Croom, M. A., Murphy, P. C., Grafton, S. B., and O'Neal, A. W., "Enabling Advanced Wind-Tunnel Research Methods Using the NASA Langley 12-Foot Low Speed Tunnel," *14th AIAA Aviation Technology, Integration, and Operations Conference*, AIAA Paper 2014-3000, Jun. 2014. https://doi.org/10.2514/6.2014-3000.

[10] Murphy, P. C., and Landman, D., "Experiment Design for Complex VTOL Aircraft with Distributed Propulsion and Tilt Wing," *AIAA Atmospheric Flight Mechanics Conference*, AIAA Paper 2015-0017, Jan. 2015. https://doi.org/10.2514/6.2015-0017.

[11] Simmons, B. M., and Murphy, P. C., "Wind Tunnel-Based Aerodynamic Model Identification for a Tilt-Wing, Distributed Electric Propulsion Aircraft," *AIAA SciTech 2021 Forum*, AIAA Paper 2021-1298, Jan. 2021. https://doi.org/10.2514/6.2021-1298.

[12] Murphy, P. C., Simmons, B. M., Hatke, D. B., and Busan, R. C., "Rapid Aero Modeling for Urban Air Mobility Aircraft in Wind-Tunnel Tests," *AIAA SciTech 2021 Forum*, AIAA Paper 2021-1644, Jan. 2021. https://doi.org/10.2514/6.2021-1644.

[13] Busan, R. C., Murphy, P. C., Hatke, D. B., and Simmons, B. M., "Wind Tunnel Testing Techniques for a Tandem Tilt-Wing, Distributed Electric Propulsion VTOL Aircraft," *AIAA SciTech 2021 Forum*, AIAA Paper 2021-1189, Jan. 2021. https://doi.org/10.2514/6.2021-1189.

[14] Hamel, P. G., and Kaletka, J., "Advances in Rotorcraft System Identification," *Progress in Aerospace Sciences*, Vol. 33, No. 3-4, 1997, pp. 259–284. https://doi.org/10.1016/S0376-0421(96)00005-X.

[15] Singleton, J. D., and Yeager, W. T., "Important Scaling Parameters for Testing Model-Scale Helicopter Rotors," *Journal of Aircraft*, Vol. 37, No. 3, 2000, pp. 396–402. https://doi.org/10.2514/2.2639.

[16] Morelli, E. A., and Klein, V., *Aircraft System Identification: Theory and Practice*, 2nd ed., Sunflyte Enterprises, Williamsburg, VA, 2016.

[17] Jategaonkar, R. V., *Flight Vehicle System Identification: A Time-Domain Methodology*, 2nd ed., American Institute of Aeronautics and Astronautics, Reston, VA, 2015. https://doi.org/10.2514/4.102790.

[18] Tischler, M. B., and Remple, R. K., *Aircraft and Rotorcraft System Identification: Engineering Methods With Flight-Test Examples*, American Institute of Aeronautics and Astronautics, Reston, VA, 2006. https://doi.org/10.2514/4.861352.

[19] Morelli, E. A., and Klein, V., "Application of System Identification to Aircraft at NASA Langley Research Center," *Journal of Aircraft*, Vol. 42, No. 1, 2005, pp. 12–25. https://doi.org/10.2514/1.3648.

[20] Hamel, P. G., and Jategaonkar, R. V., "Evolution of Flight Vehicle System Identification," *Journal of Aircraft*, Vol. 33, No. 1, 1996, pp. 9–28. https://doi.org/10.2514/3.46898.

[21] Jategaonkar, R., Fischenberg, D., and von Gruenhagen, W., "Aerodynamic Modeling and System Identification from Flight Data-Recent Applications at DLR," *Journal of Aircraft*, Vol. 41, No. 4, 2004, pp. 681–691. https://doi.org/10.2514/1.3165.

[22] Iliff, K. W., "Parameter Estimation for Flight Vehicles," *Journal of Guidance, Control, and Dynamics*, Vol. 12, No. 5, 1989, pp. 609–622. https://doi.org/10.2514/3.20454.

[23] Morelli, E. A., "Autonomous Real-Time Global Aerodynamic Modeling in the Frequency Domain," *AIAA SciTech 2020 Forum*, AIAA Paper 2020-0761, Jan. 2020. https://doi.org/10.2514/6.2020-0761.

[24] Gregory, I. M., Acheson, M. J., Bacon, B. J., Britton, T. C., Campbell, N. H., Cook, J. W., Holbrook, J. B., Moerder, D. D., Murphy, P. C., Neogi, N. A., Simmons, B. M., McMinn, J. D., and Buning, P. G., "Intelligent Contingency Management for Urban Air Mobility," *AIAA SciTech 2021 Forum*, AIAA Paper 2021-1000, Jan. 2021. https://doi.org/10.2514/6.2021-1000.

[25] Etkin, B., and Reid, L. D., *Dynamics of Flight: Stability and Control*, 3rd ed., John Wiley & Sons, Inc, New York, NY, 1996.

[26] Stevens, B. L., Lewis, F. L., and Johnson, E. N., *Aircraft Control and Simulation: Dynamics, Controls Design, and Autonomous Systems*, 3rd ed., John Wiley & Sons, Hoboken, New Jersey, 2015.

[27] Simmons, B. M., "System Identification for Propellers at High Incidence Angles," *Journal of Aircraft*, Vol. 58, No. 6, 2021, pp. 1336–1350. https://doi.org/10.2514/1.C036329.

[28] Acheson, M. J., Cook, J., and Gregory, I., "Examination of Unified Control Approaches Incorporating Generalized Control Allocation," AIAA Paper 2021-0999, Jan. 2021. https://doi.org/10.2514/6.2021-0999.

[29] Cook, J., and Gregory, I., "A Robust Uniform Control Approach for VTOL Aircraft," *VFS Autonomous VTOL Technical Meeting and Electric VTOL Symposium*, Jan. 2021.

[30] Morelli, E. A., Cunningham, K., and Hill, M. A., "Global Aerodynamic Modeling for Stall/Upset Recovery Training Using Efficient Piloted Flight Test Techniques," *AIAA Modeling and Simulation Technologies (MST) Conference*, AIAA Paper 2013-4976, Aug. 2013. https://doi.org/10.2514/6.2013-4976.

[31] Simmons, B. M., and Hatke, D. B., "Investigation of High Incidence Angle Propeller Aerodynamics for Subscale eVTOL Aircraft," NASA TM–20210014010, May 2021.

[32] Simmons, B. M., Murphy, P. C., and Busan, R. C., "Flight Dynamics Simulation and Aero-Propulsive Models for the LA-8 Tandem Tilt-Wing eVTOL Aircraft," NASA TM, In preparation.

[33] Morelli, E. A., "Multiple Input Design for Real-Time Parameter Estimation in the Frequency Domain," *13th IFAC Conference on System Identification*, Aug. 2003. https://doi.org/10.1016/S1474-6670(17)34833-4.

[34] Morelli, E. A., "Flight-Test Experiment Design for Characterizing Stability and Control of Hypersonic Vehicles," *Journal of Guidance, Control, and Dynamics*, Vol. 32, No. 3, 2009, pp. 949–959. https://doi.org/10.2514/1.37092.

[35] Morelli, E. A., "Practical Aspects of Multiple-Input Design for Aircraft System Identification Flight Tests," *AIAA AVIATION 2021 Forum*, AIAA Paper 2021-2795, Aug. 2021. https://doi.org/10.2514/6.2021-2795.

[36] Morelli, E. A., and Smith, M. S., "Real-Time Dynamic Modeling: Data Information Requirements and Flight-Test Results," *Journal of Aircraft*, Vol. 46, No. 6, 2009, pp. 1894–1905. https://doi.org/10.2514/1.40764.

[37] Montgomery, D. C., Peck, E. A., and Vining, G. G., *Introduction to Linear Regression Analysis*, 5th ed., John Wiley & Sons, Hoboken, New Jersey, 2012.

[38] Belsley, D. A., Kuh, E., and Welsch, R. E., *Regression Diagnostics: Identifying Influential Data and Sources of Collinearity*, John Wiley & Sons, Hoboken, NJ, 2004.

[39] Klein, V., "Aircraft Parameter Estimation in Frequency Domain," *4th Atmospheric Flight Mechanics Conference*, AIAA Paper 1978-1344, Aug. 1978. https://doi.org/10.2514/6.1978-1344.

[40] Morelli, E. A., and Grauer, J. A., "Practical Aspects of Frequency-Domain Approaches for Aircraft System Identification," *Journal of Aircraft*, Vol. 57, No. 2, 2020, pp. 268–291. https://doi.org/10.2514/1.C035599.

[41] Morelli, E. A., "High Accuracy Evaluation of the Finite Fourier Transform Using Sampled Data," NASA TM-110340, Jun. 1997.

[42] Morelli, E. A., "Practical Aspects of the Equation-Error Method for Aircraft Parameter Estimation," *AIAA Atmospheric Flight Mechanics Conference and Exhibit*, AIAA Paper 2006-6144, Aug. 2006. https://doi.org/10.2514/6.2006-6144.

[43] Fritsch, F. N., and Carlson, R. E., "Monotone Piecewise Cubic Interpolation," *SIAM Journal on Numerical Analysis*, Vol. 17, No. 2, 1980, pp. 238–246. https://doi.org/10.1137/0717021.

[44] Moler, C. B., *Numerical Computing with MATLAB*, Society for Industrial and Applied Mathematics, Philadelphia, PA, 2004. https://doi.org/10.1137/1.9780898717952.